RESEARCH ARTICLE

NANO · MICRO small
www.small-journal.com

Phase-dependent Friction on Exfoliated Transition Metal Dichalcogenides Atomic Layers

Dooho Lee, Hochan Jeong, Hyunsoo Lee, Yong-Hyun Kim, and Jeong Young Park**

The fundamental aspects of energy dissipation on 2-dimensional (2D) atomic layers are extensively studied. Among various atomic layers, transition metal dichalcogenides (TMDs) exists in several phases based on their lattice structure, which give rise to the different phononic and electronic contributions in energy dissipation. 2H and 1T' (distorted 1T) phase MoS_2 and $MoTe_2$ atomic layers exfoliated on mica substrate are obtained and investigated their nanotribological properties with atomic force microscopy (AFM)/ friction force microscopy (FFM). Surprisingly, 1T' phase of both MoS_2 and $MoTe_2$ exhibits ≈10 times higher friction compared to 2H phase. With density functional theory analyses, the friction increase is attributed to enhanced electronic excitation, efficient phonon dissipation, and increased potential energy surface barrier at the tip-sample interface. This study suggests the intriguing possibility of tuning the friction of TMDs through phase transition, which can lead to potential application in tunable tribological devices.

1. Introduction

At the atomic scale, the energy dissipation of friction at the surface can be mediated by the phononic contribution (eventually in the form of heat) and electronic contribution.[1] Extensive studies have been conducted on friction phenomena in 2-dimensional (2D) atomic layers.[2] Among various types of 2D atomic layers, transition metal dichalcogenides (TMDs) have received significant attention. TMDs, with the general stoichiometry of MX_2 (where M represents a transition metal and X denotes a chalcogen), exhibit unique properties. For instance, molybdenum disulfide (MoS_2), a representative TMD, naturally exists in hexagonal semiconducting 2H phase, characterized by an indirect bandgap of 1.2 eV. Conversely, the monolayer form of MoS_2 is a semiconductor with a direct bandgap of 1.9 eV.[3] Due to its 2D structure and favorable electrical properties, MoS_2 is increasingly being explored for applications in electronics, such as thin film transistors, optoelectronic devices, and flash memory.[4] Moreover, MoS_2 is widely recognized as one of the most extensively used materials in various fields as a solid lubricant,[5] with significant applications in the space industry.[6] The phase variation in MoS_2 gives rise to the distinct phononic and electronic contributions, enabling the control and tunability of friction forces. Consequently, this holds the potential to unlock new possibilities for controlling surface friction in challenging situations that demand precise regulation, such as space and other delicate environments.

During the process of lithium intercalation, electron donation from lithium induces a phase transition of MoS_2 from 2H to trigonal 1T phase, which then relaxes to 1T' (distorted 1T) phase.[7] The 1T' phase of MoS_2 persists after removal of lithium, but since 1T'-MoS_2 is metastable and converts to 2H phase by heating or aging,[8] 2H and 1T' phases coexist in lithiated MoS_2.[9] By immersing into butyllithium, Chhowalla et al.[9a,10] has successfully lithiated monolayer 2H-MoS_2 flakes, which are mechanically exfoliated or grown by chemical vapor deposition (CVD) on SiO_2 substrate, and confirmed the formation of mixed phase consisting of 2H and 1T'. In previous studies of Schumacher[11] and Scandella,[12] MoS_2 synthesized by chemical exfoliation method[13] using butyllithium exhibited friction at a similar level to mica. However, mechanically exfoliated MoS_2 from bulk 2H phase or MoS_2 grown via CVD showed significantly lower friction than mica.[14]

Atomic force microscopy (AFM)/friction force microscopy (FFM) is a powerful tool for the precise characterization of tribological properties in 2D materials.[15] Moreover, it enables the simultaneous acquisition of topographical information, such as layer thickness, providing comprehensive insight into the structural characteristics of the materials.[16] We induced a phase transition in mechanically exfoliated MoS_2 through lithiation and examined the phase-dependent tribological properties of monolayer to multilayer MoS_2 using AFM. Additionally, we investigated the friction of mechanically exfoliated 2H and 1T' phase $MoTe_2$, which belongs to the group of TMDs. Since the 1T' phase

D. Lee, H. Lee, J. Y. Park
Department of Chemistry
Korea Advanced Institute of Science and Technology (KAIST)
Daejeon 34141, Republic of Korea
E-mail: jeongypark@kaist.ac.kr
H. Jeong, Y.-H. Kim
Department of Physics
Korea Advanced Institute of Science and Technology (KAIST)
Daejeon 34141, Republic of Korea
E-mail: yong.hyun.kim@kaist.ac.kr
Y.-H. Kim
Graduate School of Nanoscience and Technology
Korea Advanced Institute of Science and Technology (KAIST)
Daejeon 34141, Republic of Korea

The ORCID identification number(s) for the author(s) of this article can be found under https://doi.org/10.1002/smll.202302713

DOI: 10.1002/smll.202302713

of $MoTe_2$ is thermodynamically stable,[17] it can exist in high purity (99.9999%) bulk crystal, which can be further exfoliated into thin 2D layers. Our results revealed that the 1T' phase of both MoS_2 and $MoTe_2$ exhibited ≈10 times higher friction than the 2H phase. These findings suggest that the phase dependence on friction is not limited to the effect of lithiation, but rather induced from the phase difference of TMDs. Density functional theory (DFT) analyses demonstrated that the phase transition from 2H to 1T' in TMDs leads to friction enhancement through enhanced electronic excitation, increased phonon density of states (DOS) overlap with the mica substrate, and an increased potential energy surface barrier. This study provides valuable insights into the atomic-level characteristics of TMDs and contributes to a deeper understanding of their fundamental properties.

2. Results and Discussion

2.1. Characterization of Lithiated MoS_2

Most TMDs, including MoS_2, naturally exist in the semiconducting 2H phase, characterized by a trigonal prismatic coordination. Through electron donation from lithium, MoS_2 in the thermodynamically stable 2H phase undergoes a phase transition to a metastable metallic 1T phase with an octahedral structure. The metastable 1T-MoS_2 improves stability by forming superlattice structures and relaxes to 1T' phase.[17b,18] **Figure 1**a,b illustrate the structures of 2H-MoS_2 and 1T'-MoS_2, respectively.

We investigated the phases of MoS_2 before and after lithiation, distinguishing them based on their different structures and electronic properties. Figure 1c shows Raman spectra of pristine 2H-MoS_2 and 1T'-MoS_2 on mica, excited by 633 nm laser. Both pristine 2H and 1T'-MoS_2 exhibited main peaks of in-plane E^1_{2g} at 381 cm^{-1}, out-of-plane A_{1g} at 406 cm^{-1}, and a longitudinal acoustic phonon peak of 2LA (M) at ≈455 cm^{-1}.[19] The shoulder of A_{1g} peak at 419 cm^{-1} is a Raman-inactive B_{1u} peak from two-phonon scattering involving a longitudinal quasi-acoustic phonon and a transverse optical phonon.[19b,20] In the Raman spectrum of 1T'-MoS_2, new peaks at 187 and 225 cm^{-1} were detected, which are consistent with the J peaks reported in previous studies on Raman spectra of 1T'-MoS_2 using a 633 nm laser as an excitation source.[21] These J peaks are attributed to the presence of a superlattice structure.[8,22] Photoluminescence (PL) spectra of 2H-MoS_2 and 1T'-MoS_2 excited by a 514 nm laser are shown in Figure 1d. The PL peaks of 2H-MoS_2 at ≈675 nm (≈1.84 eV) with a shoulder at ≈630 nm (≈1.97 eV) correspond to A and B direct excitonic transitions at the K-point in the Brillouin zone.[10,19b,23] The PL peak of 2H-MoS_2 was quenched after lithiation, indicating the phase transition of MoS_2 into a metallic 1T' phase through lithiation.[9a,10,24]

The phase composition of MoS_2 was further investigated with XPS spectra (Figure S1, Supporting Information). The XPS spectra of pristine 2H-MoS_2 exhibited sharp peaks at 229.3 and 232.5 eV, corresponding to Mo^{4+} $3d_{5/2}$ and Mo^{4+} $3d_{3/2}$ components, along with peaks at 162.3 and 163.5 eV, corresponding to S^{2-} $2p_{3/2}$ and S^{2-} $2p_{1/2}$ components, respectively.[23b,24,25] In the deconvoluted spectra of Mo 3d and S 2p orbitals for lithiated MoS_2, 1T'-MoS_2 peaks were observed, showing binding energies ≈1 eV lower than those of 2H-MoS_2.[23b,24] Friction images depicting atomic stick-slip behavior in 2H and 1T'-MoS_2 are presented in Figure 1e,f, respectively. By analyzing the Fast Fourier Transforms (FFTs) of these images, we determined the lattice constants of 2H-MoS_2 and 1T'-MoS_2 (Figure S2, Supporting Information). The 2H-MoS_2 exhibited a periodicity of ≈3.4 Å, which closely matches the lattice constant of a = 3.2 Å.[26] Meanwhile, the 1T'-MoS_2 demonstrated a periodicity of $\sqrt{3}a$ = 5.6 Å, indicative of the superlattice structure associated with the 1T' phase.[24,27]

2.2. Investigation of Tribological Properties of 2H and 1T'-MoS_2 with AFM

We employed FFM to examine the nanoscale morphology and tribology of 2H and 1T'-MoS_2. **Figure 2**a,b shows AFM topography and friction images of mechanically exfoliated pristine monolayer 2H-MoS_2 (1H-MoS_2). Line profiles of topography and friction along the red lines in the AFM images are shown in Figure 2c. The measured thickness of the exfoliated monolayer 2H-MoS_2 was 0.7–0.8 nm, showing good agreement with the theoretical value of 0.615 nm[28] and previous reports of the measured height of 2H-MoS_2 on mica substrate.[29] In the line profile, the friction values are normalized with the average measured friction value of mica in the same image. Water patches consisting of 1–2 layers of water molecules are intercalated between MoS_2 and mica, leading to an increase in the friction of MoS_2 over the water.[14] However, considering the significant difference in friction between 2H-MoS_2 and mica, the impact of this friction increase is negligible, as seen in the line profile in Figure 2c.

The topography and friction images of the 1T'-MoS_2 monolayer are shown in Figure 2d,e, respectively. The height of the monolayer 1T'-MoS_2 was 0.6–0.7 nm, which corresponds well with previously reported heights of monolayer MoS_2.[30] No water patches were observed at the 1T'-MoS_2 samples on mica substrate. Interestingly, while pristine 2H-MoS_2 exhibited significantly lower friction compared to mica, the friction of the monolayer 1T'-MoS_2 increased to a similar level with mica. At an applied load of 10 nN, the friction values of 2H and 1T'-MoS_2 were 0.12 ± 0.02 and 1.07 ± 0.07, respectively, with normalization to the value of mica. Surface roughness is known to be an important factor in determining the friction of MoS_2.[31] Figure S3 (Supporting Information) shows the root-mean-square (RMS) surface roughness (R_q) observed in the topography images of 2H and 1T'-MoS_2 in the flat area, revealing similar values of surface roughness and indicating that geometric features, such as surface roughness, are not the dominant factor contributing to the friction increase.

Contact mode AFM images of multilayer 2H and 1T'-MoS_2 under an applied load of 10 nN are presented in Figure S4 (Supporting Information). Figure S4a (Supporting Information) shows a scanned area containing bilayer to 80 nm-thick layers of 2H-MoS_2 on mica. The contrast in the friction image of Figure S4b (Supporting Information) allows the distinction of MoS_2 flakes from the mica substrate, which corresponds well with the topographic image. Slight variations in the friction of 2H-MoS_2 were observed depending on the presence of water patches intercalated between MoS_2 and mica or the thickness of the MoS_2 layers, which can be explained by the puckering effect.[2a] Nonetheless, under any conditions, multilayer MoS_2 consistently exhibited friction ≈10 times smaller than that of the mica substrate. In

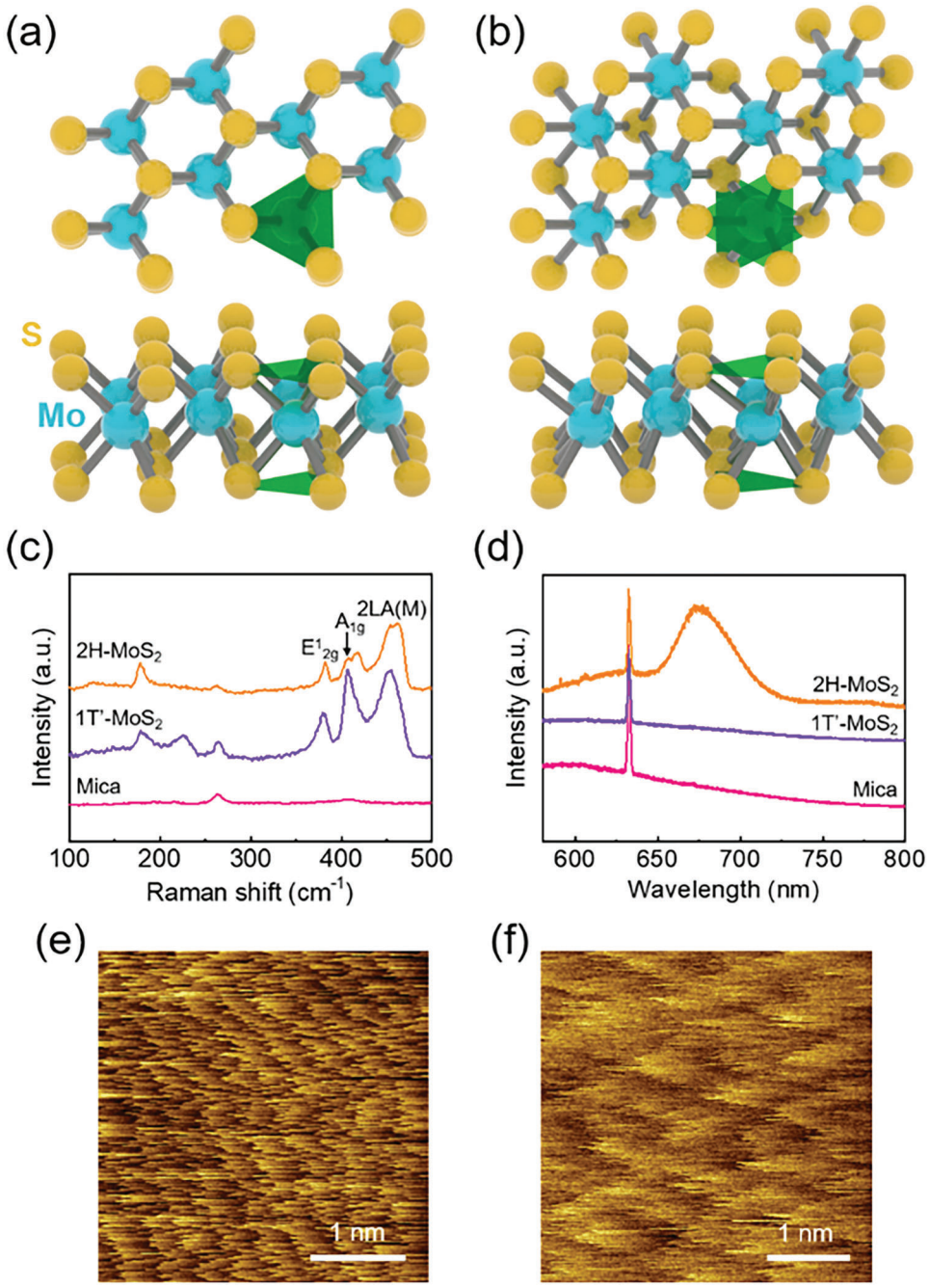

Figure 1. a) Trigonal prismatic (2H) and b) distorted octahedral (1T') phase of MoS_2. Semiconducting 2H phase can be changed into metallic 1T phase by lithiation. For group 6 TMDs, unstable ideal 1T phase improves stability by forming superlattice structure of distorted 1T phase. c) Raman spectra, and d) PL spectra of 2H-MoS_2, and 1T'-MoS_2 on mica. Friction image showing atomic stick-slip of e) 2H-MoS_2, and f) 1T'-MoS_2.

the line profile shown in Figure S4c (Supporting Information), 2H-MoS_2 layers with a thickness of ≈22 nm exhibited friction value of 0.070 ± 0.005, normalized with the average friction value of mica.

In the topographic image of multilayer 1T'-MoS_2 and mica substrate in Figure S4d (Supporting Information), wrinkles on the surface of MoS_2 can be observed. These wrinkles originate from the bulges formed during lithiation and do not reversibly shrink even after delithiation.[32] The measured height of those wrinkles depended on the thickness of the MoS_2 layers. The height of the largest wrinkle was ≈55 nm for 80 nm-thick layers of MoS_2, and ≈5 nm for 10 nm-thick layers of MoS_2. Similar to the monolayer case, if not for the high friction at the MoS_2 steps, the multilayer 1T'-MoS_2 would be difficult to distinguish from the mica substrate in the AFM friction image of Figure S4e (Supporting Information). The 6 nm-thick layers of 1T'-MoS_2 shown

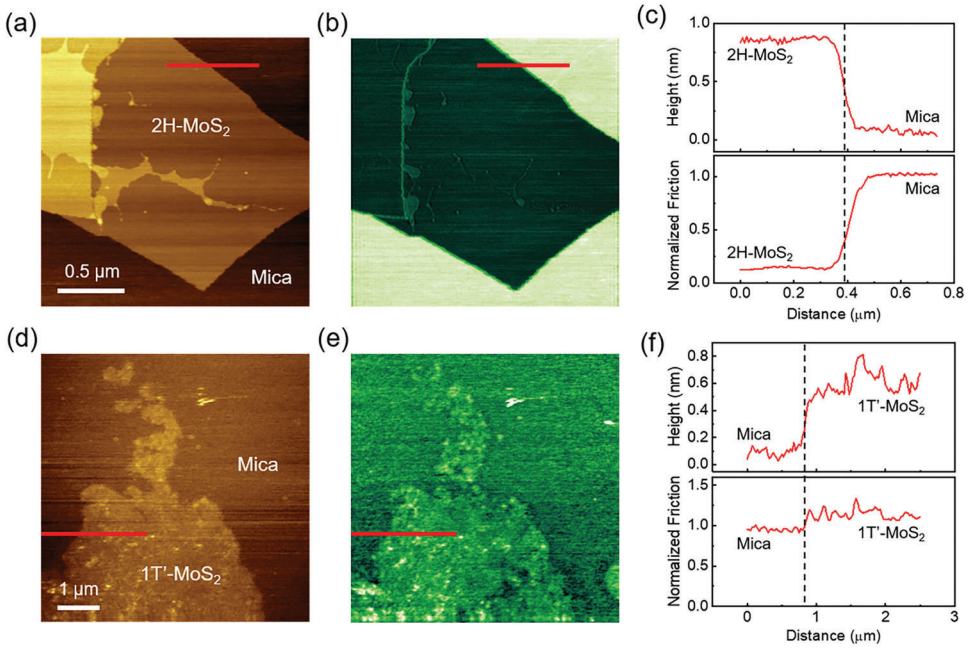

Figure 2. a) Topography and b) friction images (2 μm × 2 μm) of single layer 2H-MoS_2. c) Line profiles of height (top) and friction (bottom) along the red lines in (a,b). Friction values are normalized with the value of mica. d) Topography and e) friction images (6.4 μm × 6.4 μm) of single layer 1T'-MoS_2. f) Line profiles of height (top) and friction (bottom) along the red lines in d,e).

in Figure S4f (Supporting Information) exhibited a friction value of 1.35 ± 0.13, normalized with the friction of mica. The friction of MoS_2 was measured while avoiding large wrinkles, as those wrinkles exhibited extraordinarily high friction, due to the height differences. The friction increase resulting from lithiation displayed a similar trend at various loads. Figure S5 (Supporting Information) shows the friction plot as a function of the applied load. In order to prevent surface damage, the applied load was limited to 20 nN, as plastic deformation was observed at the edge of MoS_2 at an applied load of 30 nN. As the applied load increased, a sublinear increase in friction was observed for both mica and 1T'-MoS_2. While exfoliated 2H-MoS_2 on mica demonstrated significantly lower friction than mica under an applied load of 0–20 nN in our previous report,[14a] 1T'-MoS_2 consistently exhibited friction on a scale similar to mica for applied loads up to 20 nN.

Friction and current of 1T'-MoS_2 were evaluated as a function of applied bias using conductive AFM (Figure S6, Supporting Information). The applied bias resulted in a linear increase in current without inducing any change in friction. This observation supports the interpretation from previous reports that friction in 1T'-MoS_2 is primarily dominated by phonon excitation rather than electronic contributions involving electron-hole pair creation.[1] Force-distance spectroscopy of 1T'-MoS_2 was conducted with AFM. Figure S7a (Supporting Information) presents the adhesion and current of 1T'-MoS_2 as a function of applied bias. The adhesion of 1T'-MoS_2 exhibited minimal changes with applied bias, indicating little effect on friction. The adhesion of MoS_2 varied depending on the cantilevers used for each AFM experiment, but MoS_2 consistently exhibited similar adhesion values as mica, as shown in Figure S7b (Supporting Information). This demonstrates that the friction change induced by lithiation is not affected by different effective loads.

It is well-known that atomically thin sheets such as graphene and MoS_2 exhibit a decreasing trend in friction with increasing layer thickness on SiO_2 substrates, due to puckering effect.[2a,33] According to this study, weakly adherent SiO_2 substrates exhibit a significant decrease in friction with increasing layer thickness. However, in strongly adherent and atomically flat mica due to its high surface energy, there was little or no observed friction difference with respect to layer thickness.[34]

2.3. Phase Dependence in Tribological Properties of $MoTe_2$

In TMDs, $MoTe_2$ is known for its stable 1T' phase. To investigate the frictional properties of $MoTe_2$ and confirm that the friction change is induced by the phase transition and not solely from lithiation, we exfoliated $MoTe_2$ flakes from both 2H and 1T'-$MoTe_2$ crystals onto a mica substrate. Exfoliated 2H and 1T'-$MoTe_2$ on mica were characterized before the friction measurements. Figure S8a (Supporting Information) shows the Raman spectra of 2H and 1T'-$MoTe_2$ exfoliated on mica, using a 514 nm excitation laser. The Raman spectra of the 2H and 1T' phases of $MoTe_2$ exfoliated on mica showed characteristic peaks in good agreement with the previous studies.[35] In-plane E^1_{2g} peak at 235 cm^{-1}, out-of-plane A_{1g} peak at 174 cm^{-1}, and out-of-plane B^1_{2g} peak at 291 cm^{-1} were observed in the Raman spectra of 2H-$MoTe_2$. Successful exfoliation of 1T'-$MoTe_2$ flakes has also been confirmed by the A_g Raman modes at 132, 166, and 255 cm^{-1} (shoulder of mica peak), and B_g mode at 195 cm^{-1}.[36] The adhesion forces of both phases of $MoTe_2$ were measured using force-distance spectroscopy (Figure S8b, Supporting Informa-

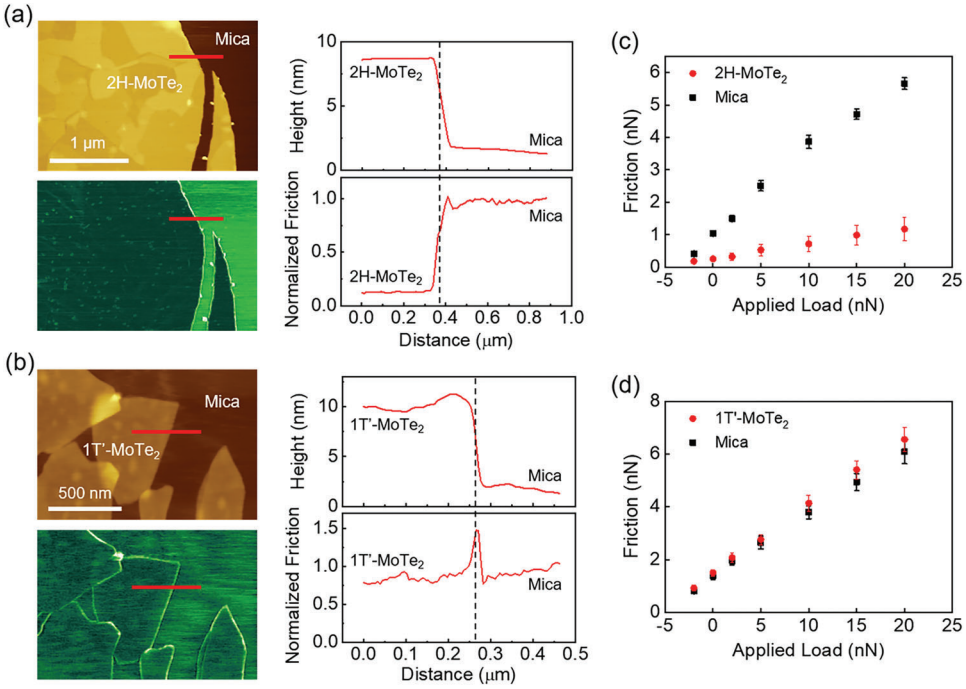

Figure 3. a) Topography and friction images (2 μm × 3 μm) of 2H-$MoTe_2$. Line profiles of height (top) and normalized friction (bottom) along the red lines in AFM images. b) Topography and friction images (1 μm × 1.5 μm) of 1T'-$MoTe_2$. Line profiles of height (top) and normalized friction (bottom) along the red lines in AFM images. c) Friction of 2H-$MoTe_2$ and mica as a function of applied load. d) Friction of 1T'-$MoTe_2$ and mica as a function of applied load.

tion). Both phases of $MoTe_2$ exhibited similar adhesion forces with mica, indicating that the effective load difference did not affect the friction of $MoTe_2$.

The tribological properties of 2H and 1T'-$MoTe_2$ on mica were investigated using contact mode AFM. **Figure 3**a,b shows the AFM topography and friction images of 2H and 1T'-$MoTe_2$, with the line profile along the red line in the image. An applied load of 10 nN was used to obtain these images. In the friction image of 2H-$MoTe_2$ with a thickness of ≈6.9 nm, the shape of $MoTe_2$ is distinguishable from mica, and the contrast matches well with the topography, similar to MoS_2. Intercalated water patches with heights of ≈0.4 nm were also observed in the AFM image of 2H-$MoTe_2$. On the other hand, the friction of ≈8.1 nm-thick 1T'-$MoTe_2$ is almost equivalent to that of mica, except at the step edges.

For 2H-$MoTe_2$, the first layer on SiO_2 was ≈0.9 nm thick, followed by subsequent layers with a thickness of 0.7 nm.[37] For 1T'-$MoTe_2$, the monolayer on SiO_2 exhibited a thickness of 0.82 nm.[38] In our experiment, the observed thickness of 2H-$MoTe_2$ was ≈6.9 nm, indicating a flake consisting of ≈9 ± 1 layers. For 1T'-$MoTe_2$, the thickness was ≈8.1 nm, suggesting a flake composed of ≈11 ± 1 layers.

The friction of 2H and 1T'-$MoTe_2$ on mica as a function of applied load is shown in Figure 3c,d. Both phases of $MoTe_2$ exhibit a sublinear increase in friction as the applied load increases, demonstrating similar frictional properties up to an applied load of 20 nN. At an applied load of 10 nN, when normalized to the friction value of mica, the friction values of 2H and 1T'-$MoTe_2$ are 0.18 ± 0.06 and 1.09 ± 0.08, respectively. The friction characteristics of the $MoTe_2$ flakes in our experiment, which have a thickness of ≈10 layers, can be considered "bulk-like" since the substrate effect is known to start diminishing from ≈6 layers.[39] 2H-$MoTe_2$ is known to exhibit slightly lower friction than 2H-MoS_2 at atomic scale,[40] but it should be noted that the friction values between MoS_2 and $MoTe_2$ in our experiment cannot be quantitatively compared due to the different scanning conditions.

Experiments using a different tip showed similar observations where 1T'-$MoTe_2$ showed much higher friction than 2H-$MoTe_2$, ruling out the potential effect of tip contamination (Figure S9, Supporting Information). We note that our result is in contrast to the earlier work on WS_2,[41] where WS_2 in the 1T phase exhibits lower friction then the 2H phase. Because the fluorination was utilized to induce phase transition, this is a different case from our studies where mechanically exfoliated $MoTe_2$ were used.

2.4. DFT Calculations of MoS_2 and $MoTe_2$

To understand the difference in friction between the 2H and 1T' phases, we performed DFT calculations for monolayer MoS_2 and $MoTe_2$. The optimized structures of 2H and 1T' phases in MoS_2 and $MoTe_2$ are shown in Figure S10 (Supporting Information). 2H phase shows trigonal prismatic coordination with the identical Mo-S (or Te) bond lengths. However, 1T' phase shows distorted octahedral coordination with different Mo-S (or Te) bond lengths and Mo-Mo dimerization. From the electronic band structures in **Figure 4**a,b, 2H-MoS_2 is a of 1.75 eV, and 1T'-MoS_2 shows a small bandgap of 0.03 eV. Similarly, 2H-$MoTe_2$ is semiconducting with a bandgap of 1.50 eV, while 1T'-$MoTe_2$ is metallic with no bandgap (**Figure 5**a,b). Our calculated results

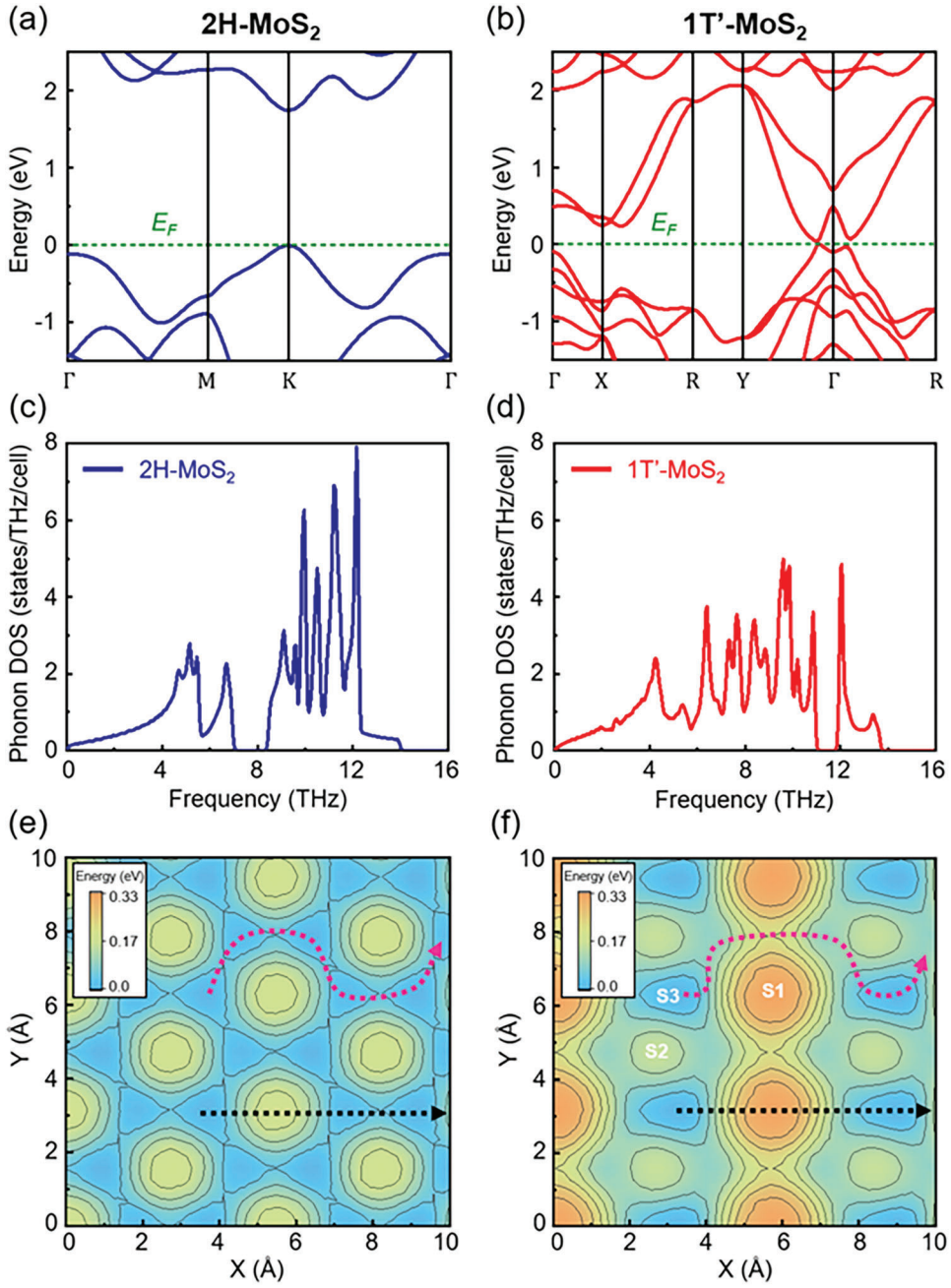

Figure 4. Electronic band structures of a) 2H-MoS_2 and b) 1T'-MoS_2. Fermi energy is set to 0 eV (green dotted line). Phonon density of states (DOS) of c) 2H-MoS_2 and d) 1T'-MoS_2. Potential energy surfaces of e) 2H-MoS_2 and f) 1T'-MoS_2. The dotted lines indicate the scanning directions for the maximum (black) and minimum (red) barriers.

are in good agreement with other reported calculations.[42] As frictional excitation could be initiated by small electronic excitations at its early stage, the 2H phase may not allow such electronic excitations, due to its large bandgap. On the other hand, the metallic 1T' phases can significantly host electronic excitations for the dissipation of frictional energy, such as electron-hole pairs by excitation at a short time scale, which later turn into phononic excitations, resulting in increased frictional force. However, since the electron contribution effect associated with energy dissipation is likely minor considering the values of measured friction,[43] we considered other factors affecting frictional forces, such as phonons and potential energy barriers.

Lattice vibrational energy can be a main source for energy dissipation in solid interfaces. Frictional force is closely related to phonon dissipation and can be understood as phonon DOS in 2D materials.[14b,44] The phonon DOS' of 2H and 1T'-MoS_2 in Figure 4c,d, are primarily distributed between 0 and 14 THz. In details, however, the phonon DOS of 1T'-MoS_2 is quite different

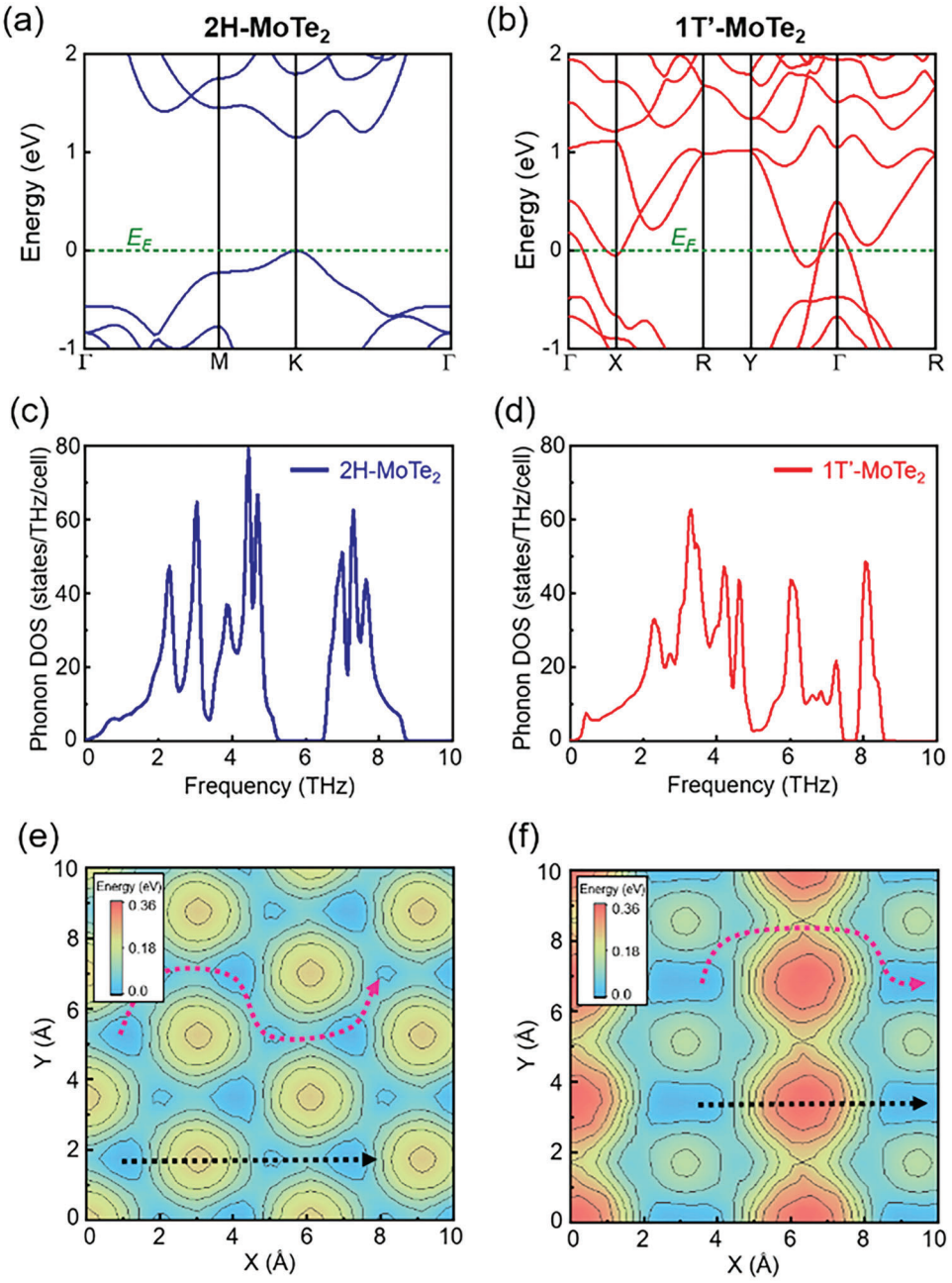

Figure 5. Electronic band structures of monolayer a) 2H-$MoTe_2$ and b) 1T'-$MoTe_2$. Fermi energy is set to 0 eV (green dotted line). Projected phonon density of states (DOS) of c) 2H-$MoTe_2$ and d) 1T'-$MoTe_2$ on mica substrate. Weak vdW interaction by the effect of the substrate shows a small DOS protrusion below 1THz. Potential energy surfaces of e) 2H-$MoTe_2$ and f) 1T'-$MoTe_2$. The dotted lines indicate the scanning directions for the maximum (black) and minimum (red) barriers.

from 2H-MoS_2, because all bond lengths and symmetry varied from 2H phase to 1T' phase. 2H-MoS_2 shows a large phonon gap of 1.20 THz above 7.1 THz between acoustic and optical phonon modes.

On the other hand, 1T'-MoS_2 provide continuous phonon excitation channels below 11 THz with a small gap of 0.65 THz above 11.1 THz. This phonon distribution can efficiently promote the dissipation of frictional energy within the bulk monolayer of 1T'-MoS_2. Since phonons can dissipate into the substrate, we considered slab models of 2H/1T'-MoS_2 on a mica substrate (Figure S11a,b, Supporting Information). The interlayer distance and binding energy were 2.98 Å and 0.158 eV (/MoS_2 unit) for 2H-MoS_2 and 2.88 Å and 0.157 eV for 1T'-MoS_2. The binding energy and interlayer distance were nearly similar in 2H/1T' phases. In addition, there was minor phonon DOS protrusion below 1 THz by the substrate (Figure S11c, Supporting Information), indicating that there were no chemical bonds between 2H/1T'-MoS_2 and mica, but only weak vdW interactions. As a result, in the

low-frequency region (especially below 4 THz), the 1T'-MoS_2 has a higher phonon DOS than the 2H-MoS_2, which suggests that phonon in 1T'-MoS_2 can be more efficiently dissipated toward mica substrate via phonon DOS overlap.[14b] Similarly, for $MoTe_2$ on mica, as shown in Figure 5, 2H-$MoTe_2$ exhibits a large phonon gap of 1.1 THz over 5.3 THz, whereas 1T'-$MoTe_2$ shows a small gap of 0.25 THz above 7.5 THz, as well as higher phonon DOS below 4 THz than 2H-$MoTe_2$. Not only does 1T' phase exhibit significant phonon DOS overlap with mica, but it also shows continuous phonon excitation channels with small phonon gap. It means that 1T' phase has better phonon transport toward substrate and more frictional energy dissipation compared to 2H phase. Therefore, the phonon energy dissipation scenario also supports why 1T' phase has a larger frictional force than 2H phase.

Lastly, we calculated the van der Waals (vdW) interactions of the scanning tip on monolayer MoS_2. In the classical Prandtl-Tomlinson (PT) model[45] and related simulations,[46] it is well known that frictional force at the atomic scale is proportional to the height of the potential energy surface barrier. This is because the high energy barrier prevents the tip from easily slipping and pushes it to accumulate more lateral forces.

Figure 4e,f shows the potential energy surfaces (PES) when the Si cluster tip moves on the 2H-MoS_2 and 1T'-MoS_2 surfaces. To obtain the potential energy surface, we performed total energy calculation by using a hydrogen passivated Si cluster tip ($Si_{10}H_{16}$) on the (5×3) supercell of orthorhombic MoS_2 unit cell. Per the orthorhombic unit cell, we used ≈200 fine grid points to find the most stable configurations in each point. The center of the tip was fixed in each position while the height of the tip and other atoms were fully relaxed. The vdW equilibrium distance was optimized at each tip location, and the lowest energy sites were shifted to 0 eV for references. In 2H-MoS_2, the lowest energy site is the Mo site and the highest energy site is S site. In 1T'-MoS_2, however, the lowest energy site is the bottom sulfur site (S3 site). The transition from trigonal (2H) to octahedral (1T') symmetry increases the interatomic distance between Mo and Mo atoms and causes height variation (≈0.4 Å) of sulfur atoms in 1T'-MoS_2, as shown in Figure S10 (Supporting Information). This structural distortion enabled the tip to probe deeper on the 1T'-MoS_2 surface and enhanced its vdW interactions with adjacent atoms. As a result, the energy barrier for 1T'-MoS_2 can be higher than for 2H-MoS_2.

Along the straight scanning direction (black dotted line), we calculated the maximum energy barriers equal to 0.19 eV for 2H-MoS_2 (Figure 4e) and 0.33 eV for 1T'-MoS_2 (Figure 4f). This can explain why 1T' can have a higher frictional force than 2H. Furthermore, it is well known that an elastic tip can deviate from the sulfur atom with the highest energy and detour to the saddle point with a lower energy during a slip motion.[40] Thus, we also obtained the minimum energy barriers (red dotted line) in Figure 4e,f. The 1T'-MoS_2 shows significantly higher energy barrier (0.21 eV) than for 2H-MoS_2 (0.041 eV), indicating the greater friction in 1T'-MoS_2. Figure S13 (Supporting Information) provides specific details about the barriers. Likewise, the similar trend is confirmed in the PES and energy barrier of $MoTe_2$ (Figure 5). The minimum (maximum) energy barrier of 2H-$MoTe_2$ is 0.067 eV (0.24 eV), whereas that of 1T'-$MoTe_2$ is 0.22 eV (0.35 eV). In both MoS_2 and $MoTe_2$, the 1T' phase exhibits a higher energy barrier than 2H phase, which can result in friction increase.

From the results of electronic bands, phonon DOS, and PES, we could speculate why the 1T' phase exhibits a larger friction than the 2H phase. The generated mechanical energy can be dissipated more efficiently in 1T' phase by the facile electron and phonon excitations. Also, when the tip moves on the surface of 1T' phase, large frictional force is required to overcome the potential energy surface barrier during scanning motion.

3. Conclusion

In summary, we investigated the effect of phase transition on the nanotribological properties of TMDs using friction force microscopy. Specifically, we examined the hexagonal semiconducting 2H phase and the distorted 1T' phase of exfoliated MoS_2 and $MoTe_2$ atomic layers on a mica substrate. Our findings demonstrate that the 1T' phase of both MoS_2 and $MoTe_2$, formed through lithiation or exfoliation, exhibits approximately ten times higher friction compared to the 2H phase. Through DFT analysis, we were able to establish a connection between this phenomenon and fundamental differences in electronic, phononic, and PES structures between the two phases, which impact energy transfer. Our study highlights the potential for controlling the tribological properties of TMDs through phase transition.

4. Experimental Section

Sample Preparation: 2H-MoS_2 (2D semiconductors) flakes were prepared on freshly cleaved muscovite mica (Ted Pella, Inc.) by mechanical exfoliation using adhesive Scotch tape at ambient conditions (20–40% relative humidity (RH), 23–24°C). The phase transition from 2H-MoS_2 to 1T'-MoS_2 was performed by lithiation by immersing MoS_2 on mica samples in n-butyllithium solution (1.6 M in hexane, Sigma-Aldrich) for 2 h. The sample was then washed with hexane (Sigma-Aldrich) and deionized water to remove the excess butyllithium and the remaining lithium cations. The lithiation process was performed in the glove box with N_2 atmosphere. 2H-$MoTe_2$ (2D semiconductors) and 1T'-$MoTe_2$ (2D semiconductors) flakes were also mechanically exfoliated on freshly cleaved muscovite mica, using adhesive tape at 15–20% RH, 21–22 °C.

Characterization: Raman and PL spectra of different phases of MoS_2 and $MoTe_2$ were carried out with a dispersive Raman spectrometer (ARAMIS, Horiba Jobin Yvon) using 514 and 633 nm laser at room temperature. Raman spectra were calibrated with 521 cm^{-1} silicon band. X-ray photoelectron spectroscopy (XPS) spectra of 2H-MoS_2 and 1T'-MoS_2 were measured by Sigma Probe, Thermo VG Scientific using Al Kα X-ray as excitation source (1486.7 eV). The C 1s peak at 284.8 eV was used as the reference for the calibration of XPS spectra.

AFM Measurements: Contact mode AFM measurements were performed at air and room temperature with Keysight 5500 AFM. Silicon cantilever (PPP-LFMR, Nanosensors) with a spring constant of 0.2 N m^{-1} and tip radius < 10 nm was used for lateral force microscopy (LFM), and silicon cantilever with an electrically conductive coating of 5 nm chromium and 25 nm platinum (ContE-G, Budgetsensors) with spring constant of 0.2 N m^{-1} and tip radius < 25 nm was used for conductive AFM (C-AFM) measurements. The wedge method[47] was employed for the friction calibration of the cantilever using TGF11 calibration grating by MikroMasch. The AFM scan images in the range of 1.5 to 25 µm, as shown in the manuscript and Supporting Information, were acquired using scan rates ranging from 3.84 to 18.03 µm s^{-1}.

Computational Method: First-principles DFT calculations were performed using the Vienna Ab initio Simulation Package (VASP).[48] For

the interaction of valence electrons, the projector augmented wave (PAW) method[49] and the plane wave energy cutoff of 500 eV were used. All atomic structures were optimized with Perdew, Burke, and Ernzerhof (PBE) exchange correlation functional[50] with dispersion-corrected DFT-D3 method of Grimme (PBE-D3). For the ionic relaxation, atomic forces were minimized until the force criterion was less than 0.01 eV $Å^{-1}$ (0.001 eV $Å^{-1}$ for phonon). The orthorhombic cells ($a \times \sqrt{3}a$; $a = 3.161$ Å) for monolayer 2H/1T'-MoS_2 (or $MoTe_2$) were used at vacuum separation of ≈15 Å in the z-direction. In a slab model of MoS_2 on mica, a (3×2) supercell of MoS_2 and a (1×2) supercell of mica ($a = 9.15$ Å, $b = 5.28$ Å) were used. Because the strain effect of MoS_2 is not the interest, a lattice constant of the slab model was just fixed to MoS_2. The phonon calculations were performed using the finite displacement method[51] implemented in the Phonopy program.[52]

Supporting Information

Supporting Information is available from the Wiley Online Library or from the author.

Acknowledgements

This research was supported by an internal project of Korea Institute of Science and Technology (KIST), and Basic Science Research Program through the National Research Foundation of Korea (NRF) funded by the Ministry of Education (2019R1A6A1A10073887), and funded by the Korean government (MSIT) (2022R1A2C3004242).

Conflict of Interest

The authors declare no conflict of interest.

Author Contributions

D.L. and H.J. contributed equally to this work. D.L. and H.L. fabricated samples, performed optical spectroscopy, AFM measurements and data analysis under J.Y.P.'s supervision. H.J. performed DFT calculations and analysis under Y.-H.K.'s supervision. D.L., H.J., Y.-H.K. and J.Y.P. wrote the manuscript.

Data Availability Statement

The data that support the findings of this study are available from the corresponding author upon reasonable request.

Keywords

atomic force microscopy (AFM), density functional theory (DFT), molybdenum, phase transition, tribology

Received: March 30, 2023
Revised: July 7, 2023
Published online: July 23, 2023

[1] J. Y. Park, M. Salmeron, *Chem. Rev.* **2013**, *114*, 677.
[2] a) C. Lee, Q. Li, W. Kalb, X.-Z. Liu, H. Berger, R. W. Carpick, J. Hone, *Science* **2010**, *328*, 76; b) S. Kwon, J.-H. Ko, K.-J. Jeon, Y.-H. Kim, J. Y. Park, *Nano Lett.* **2012**, *12*, 6043.
[3] a) A. Kuc, N. Zibouche, T. Heine, *Phys. Rev. B* **2011**, *83*, 245213; b) K. F. Mak, C. Lee, J. Hone, J. Shan, T. F. Heinz, *Phys. Rev. Lett.* **2010**, *105*, 136805.
[4] a) G.-H. Lee, Y.-J. Yu, X. Cui, N. Petrone, C.-H. Lee, M. S. Choi, D.-Y. Lee, C. Lee, W. J. Yoo, K. Watanabe, *ACS Nano* **2013**, *7*, 7931; b) B. Radisavljevic, A. Radenovic, J. Brivio, V. Giacometti, A. Kis, *Nat. Nanotechnol.* **2011**, *6*, 147; c) S. Bertolazzi, D. Krasnozhon, A. Kis, *ACS Nano* **2013**, *7*, 3246; d) O. Lopez-Sanchez, D. Lembke, M. Kayci, A. Radenovic, A. Kis, *Nat. Nanotechnol.* **2013**, *8*, 497; e) D. Lembke, S. Bertolazzi, A. Kis, *Acc. Chem. Res.* **2015**, *48*, 100.
[5] M. R. Vazirisereshk, A. Martini, D. A. Strubbe, M. Z. Baykara, *Lubricants* **2019**, *7*, 57.
[6] E. Roberts, *Thin Solid Films* **1989**, *181*, 461.
[7] H. Shu, F. Li, C. Hu, P. Liang, D. Cao, X. Chen, *Nanoscale* **2016**, *8*, 2918.
[8] D. Yang, S. J. Sandoval, W. Divigalpitiya, J. Irwin, R. Frindt, *Phys. Rev. B* **1991**, *43*, 12053.
[9] a) R. Kappera, D. Voiry, S. E. Yalcin, B. Branch, G. Gupta, A. D. Mohite, M. Chhowalla, *Nat. Mater.* **2014**, *13*, 1128; b) G. Eda, T. Fujita, H. Yamaguchi, D. Voiry, M. Chen, M. Chhowalla, *ACS Nano* **2012**, *6*, 7311.
[10] R. Kappera, D. Voiry, S. E. Yalcin, W. Jen, M. Acerce, S. Torrel, B. Branch, S. Lei, W. Chen, S. Najmaei, J. Lou, P. M. Ajayan, G. Gupta, A. D. Mohite, M. Chhowalla, *APL Mater.* **2014**, *2*, 092516.
[11] A. Schumacher, N. Kruse, R. Prins, E. Meyer, R. Lüthi, L. Howald, H. J. Güntherodt, L. Scandella, *J. Vac. Sci. Technol., B: Microelectron. Nanometer Struct. Process. Meas., Phenom.* **1996**, *14*, 1264.
[12] L. Scandella, A. Schumacher, N. Kruse, R. Prins, E. Meyer, R. Lüthi, L. Howald, H. J. Güntherodt, *Thin Solid Films* **1994**, *240*, 101.
[13] a) P. Joensen, R. Frindt, S. R. Morrison, *Mater. Res. Bull.* **1986**, *21*, 457; b) A. Schumacher, L. Scandella, N. Kruse, R. Prins, *Surf. Sci.* **1993**, *289*, L595.
[14] a) D. Lee, H. Lee, H. Lee, J. Y. Park, *J. Phys. Chem. C* **2020**, *124*, 16902; b) H. Lee, H. Jeong, J. Suh, W. H. Doh, J. Baik, H.-J. Shin, J.-H. Ko, J. Wu, Y.-H. Kim, J. Y. Park, *J. Phys. Chem. C* **2019**, *123*, 8827.
[15] a) R. W. Carpick, M. Salmeron, *Chem. Rev.* **1997**, *97*, 1163; b) F. J. Giessibl, *Rev. Mod. Phys.* **2003**, *75*, 949.
[16] S. Kwon, K. E. Lee, H. Lee, S. J. Koh, J.-H. Ko, Y.-H. Kim, S. O. Kim, J. Y. Park, *J. Phys. Chem. B* **2018**, *122*, 543.
[17] a) M. Kan, H. G. Nam, Y. H. Lee, Q. Sun, *Phys. Chem. Chem. Phys.* **2015**, *17*, 14866; b) K.-A. N. Duerloo, Y. Li, E. J. Reed, *Nat. Commun.* **2014**, *5*, 4214; c) S. Song, D. H. Keum, S. Cho, D. Perello, Y. Kim, Y. H. Lee, *Nano Lett.* **2016**, *16*, 188.
[18] Y. Guo, D. Sun, B. Ouyang, A. Raja, J. Song, T. F. Heinz, L. E. Brus, *Nano Lett.* **2015**, *15*, 5081.
[19] a) B. C. Windom, W. Sawyer, D. W. Hahn, *Tribol. Lett.* **2011**, *42*, 301; b) H. Li, Q. Zhang, C. C. R. Yap, B. K. Tay, T. H. T. Edwin, A. Olivier, D. Baillargeat, *Adv. Funct. Mater.* **2012**, *22*, 1385; c) V. Vuong, C. Hung, *Commun. Phys.* **2018**, *28*, 379.
[20] T. Sekine, K. Uchinokura, T. Nakashizu, E. Matsuura, R. Yoshizaki, *J. Phys. Soc. Jpn.* **1984**, *53*, 811.
[21] a) E. Er, H.-L. Hou, A. Criado, J. Langer, M. Möller, N. Erk, L. M. Liz-Marzán, M. Prato, *Chem. Mater.* **2019**, *31*, 5725; b) M. Wu, J. Zhan, K. Wu, Z. Li, L. Wang, B. Geng, L. Wang, D. Pan, *J. Mater. Chem. A* **2017**, *5*, 14061; c) A. A. Jeffery, S. R. Rao, M. Rajamathi, *Carbon* **2017**, *112*, 8; d) M. A. Koklioti, C. Bittencourt, X. Noirfalise, I. Saucedo-Orozco, M. Quintana, N. Tagmatarchis, *ACS Appl. Nano Mater.* **2018**, *1*, 3625.
[22] S. J. Sandoval, D. Yang, R. Frindt, J. Irwin, *Phys. Rev. B* **1991**, *44*, 3955.
[23] a) A. Splendiani, L. Sun, Y. Zhang, T. Li, J. Kim, C.-Y. Chim, G. Galli, F. Wang, *Nano Lett.* **2010**, *10*, 1271; b) G. Eda, H. Yamaguchi, D. Voiry, T. Fujita, M. Chen, M. Chhowalla, *Nano Lett.* **2011**, *11*, 5111.
[24] Y. Yu, G.-H. Nam, Q. He, X.-J. Wu, K. Zhang, Z. Yang, J. Chen, Q. Ma, M. Zhao, Z. Liu, F.-R. Ran, X. Wang, H. Li, X. Huang, B. Li, Q. Xiong,

Q. Zhang, Z. Liu, L. Gu, Y. Du, W. Huang, H. Zhang, *Nat. Chem.* **2018**, *10*, 638.
[25] a) C. Zhang, Z. Wang, S. Bhoyate, T. Morey, B. L. Neria, V. Vasiraju, G. Gupta, S. Palchoudhury, P. Kahol, S. Mishra, F. Perez, R. K. Gupta, *C* **2017**, *3*, 33; b) B. Li, L. Jiang, X. Li, P. Ran, P. Zuo, A. Wang, L. Qu, Y. Zhao, Z. Cheng, Y. Lu, *Sci. Rep.* **2017**, *7*, 11182.
[26] a) O. K. Le, V. Chihaia, M.-P. Pham-Ho, *RSC Adv.* **2020**, *10*, 4201; b) A. Molina-Sanchez, L. Wirtz, *Phys. Rev. B* **2011**, *84*, 155413.
[27] T. Hu, R. Li, J. Dong, *J. Chem. Phys.* **2013**, *139*, 174702.
[28] R. Frindt, *J. Appl. Phys.* **1966**, *37*, 1928.
[29] a) Q. Ji, Y. Zhang, T. Gao, Y. Zhang, D. Ma, M. Liu, Y. Chen, X. Qiao, P.-H. Tan, M. Kan, *Nano Lett.* **2013**, *13*, 3870; b) J. O. Varghese, P. Agbo, A. M. Sutherland, V. W. Brar, G. R. Rossman, H. B. Gray, J. R. Heath, *Adv. Mater.* **2015**, *27*, 2734.
[30] a) Y. Li, K. Chang, Z. Sun, E. Shangguan, H. Tang, B. Li, J. Sun, Z. Chang, *ACS Appl. Energy Mater.* **2019**, *3*, 998; b) S. Shi, Z. Sun, Y. H. Hu, *J. Mater. Chem. A* **2018**, *6*, 23932.
[31] J. Quereda, A. Castellanos-Gomez, N. Agraït, G. Rubio-Bollinger, *Appl. Phys. Lett.* **2014**, *105*, 053111.
[32] J. Wan, Y. Hao, Y. Shi, Y.-X. Song, H.-J. Yan, J. Zheng, R. Wen, L.-J. Wan, *Nat. Commun.* **2019**, *10*, 3265.
[33] J. S. Choi, J.-S. Kim, I.-S. Byun, D. H. Lee, M. J. Lee, B. H. Park, C. Lee, D. Yoon, H. Cheong, K. H. Lee, *Science* **2011**, *333*, 607.
[34] T. W. Go, D. Lee, W. Choi, J. Y. Park, *J. Vac. Sci. Technol., A* **2021**, *39*, 060803.
[35] J. P. Fraser, L. Masaityte, J. Zhang, S. Laing, J. C. Moreno-López, A. F. McKenzie, J. C. McGlynn, V. Panchal, D. Graham, O. Kazakova, T. Pichler, D. A. MacLaren, D. A. J. Moran, A. Y. Ganin, *Commun. Mater.* **2020**, *1*, 48.
[36] L. Zhou, S. Huang, Y. Tatsumi, L. Wu, H. Guo, Y.-Q. Bie, K. Ueno, T. Yang, Y. Zhu, J. Kong, R. Saito, M. Dresselhaus, *J. Am. Chem. Soc.* **2017**, *139*, 8396.
[37] a) M. Yamamoto, S. T. Wang, M. Ni, Y.-F. Lin, S.-L. Li, S. Aikawa, W.-B. Jian, K. Ueno, K. Wakabayashi, K. Tsukagoshi, *ACS Nano* **2014**, *8*, 3895; b) J.-H. Li, D. Bing, Z.-T. Wu, G.-Q. Wu, J. Bai, R.-X. Du, Z.-Q. Qi, *Chin. Phys. B* **2020**, *29*, 017802.
[38] S. Pace, L. Martini, D. Convertino, D. H. Keum, S. Forti, S. Pezzini, F. Fabbri, V. Miseikis, C. Coletti, *ACS Nano* **2021**, *15*, 4213.
[39] J. Yang, L. Liu, *Appl. Surf. Sci.* **2020**, *502*, 144402.
[40] M. R. Vazirisereshk, K. Hasz, M.-Q. Zhao, A. C. Johnson, R. W. Carpick, A. Martini, *ACS Nano* **2020**, *14*, 16013.
[41] S. Radhakrishnan, D. Das, L. Deng, P. M. Sudeep, G. Colas, C. A. de Los Reyes, S. Yazdi, C. W. Chu, A. A. Martí, C. S. Tiwary, *Adv. Mater.* **2018**, *30*, 1803366.
[42] a) X. Qian, J. Liu, L. Fu, J. Li, *Science* **2014**, *346*, 1344; b) Z.-Y. Zhao, Q.-L. Liu, *Catal. Sci. Technol.* **2018**, *8*, 1867.
[43] a) M. Kisiel, E. Gnecco, U. Gysin, L. Marot, S. Rast, E. Meyer, *Nat. Mater.* **2011**, *10*, 119; b) J. Y. Park, D. Ogletree, P. Thiel, M. Salmeron, *Science* **2006**, *313*, 186; c) Y. Qi, J. Park, B. Hendriksen, D. Ogletree, M. Salmeron, *Phys. Rev. B* **2008**, *77*, 184105.
[44] H. Lee, J.-H. Ko, J. S. Choi, J. H. Hwang, Y.-H. Kim, M. Salmeron, J. Y. Park, *J. Phys. Chem. Lett.* **2017**, *8*, 3482.
[45] a) L. Prandtl, *Z. Angew. Math. Mech.* **1928**, *8*, 85; b) G. Tomlinson, *London, Edinburgh Dublin Philos. Mag. J. Sci.* **1929**, *7*, 905.
[46] a) M. R. Vazirisereshk, H. Ye, Z. Ye, A. Otero-de-la-Roza, M.-Q. Zhao, Z. Gao, A. C. Johnson, E. R. Johnson, R. W. Carpick, A. Martini, *Nano Lett.* **2019**, *19*, 5496; b) M. R. Vazirisereshk, K. Hasz, R. W. Carpick, A. Martini, *J. Phys. Chem. Lett.* **2020**, *11*, 6900.
[47] M. Varenberg, I. Etsion, G. Halperin, *Rev. Sci. Instrum.* **2003**, *74*, 3362.
[48] G. Kresse, J. Furthmüller, *Phys. Rev. B* **1996**, *54*, 11169.
[49] P. E. Blöchl, *Phys. Rev. B* **1994**, *50*, 17953.
[50] J. P. Perdew, K. Burke, M. Ernzerhof, *Phys. Rev. Lett.* **1996**, *77*, 3865.
[51] G. Kresse, J. Furthmüller, J. Hafner, *EPL* **1995**, *32*, 729.
[52] A. Togo, F. Oba, I. Tanaka, *Phys. Rev. B* **2008**, *78*, 134106.